Proceedings of ICFDP7:
Seventh International Congress on Fluid Dynamics & Propulsion
December 18-20, 2001, Cairo, Egypt

ICFDP7-2001022

EXPERIMENTAL AND NUMERICAL STUDY OF TURBULENT WAKE FLOW BEHIND PERFORATED DISKS

Richard J. M. Messiha and Ahmed R. El-Baz
Mechanical Power Engineering Department,
Ain Shams University, Cairo 11517, Egypt

Mohamed A. E. Selim
Civil Aviation Institute, Giza, Egypt

ABSTRACT

A subsonic air-tunnel study was undertaken for the investigation of the aerodynamic characteristics of the axisymmetric turbulent wake flow behind perforated circular disks. Such geometric alteration is suggested as a means for flow control in bluff body wakes. Experimental measurements were carried out using three perforated disks, each of 30 mm diameter. The central-hole to disk diameter ratios were 0.17, 0.27 and 0.37. Mean velocities and root-mean-square of turbulence intensities, up to 8 disk diameters, have been measured with a constant-temperature hot-wire anemometer. For all observations, the Reynolds number of the undisturbed oncoming flow (based on the disk diameter) was around 3.6×10^4. The performance of a two-equation turbulence model in conjunction with a finite-volume-based numerical prediction procedure was tested for selected previous experimental data for solid disks. Computations for the flow behind perforated disks were also performed using the standard k-ε model and two variants of it accounting for the effects of the streamlines curvature. Numerical results are in reasonable agreement with experimental measurements.

1. INTRODUCTION

The separated recirculating flow which is established in the lee of bluff or unstreamlined bodies has direct engineering significance. For instance, such a flow regime can be used to stabilize flames in high-velocity reactant streams. The details of the aerodynamics of the near wake of the bluff body are crucial to the description of the mechanisms of stabilization. For example, the size of the recirculation zone affects the ability of production of hot burnt products, and the mixing between these products and the reactants is governed by the turbulence in the free shear layers surrounding the rear region. The study of isothermal models of the reacting flow allows much to be learnt about the near wake in experimentally, and conceptually, simpler flows.

Despite the fact that the study of bluff-body flows has been a subject of interest to engineers as well as to scientists for several decades, an understanding of the flow behind a bluff body poses a great challenge. The complexity of bluff- body flows is a direct consequence of the fact that these flows involve the interactions of three shear layers in the same problem, namely a boundary layer, a separating free shear layer and a wake. As has been recently remarked by [1], "the problem of bluff body flow remains almost entirely in the empirical, descriptive realm of knowledge, although our knowledge of this flow is extensive". In fact, the recent surge of activity on wakes over the past decade from experiment, direct numerical simulation and analysis has yielded a wealth of new understandings.

A turbulent wake is generally divided into three regions, namely (1) near-wake, (2) transition and (3) similarity or far-wake. The near-wake region, where periodic vortex streets are formed, is dominated by the mixing process associated with the free shear layer that results from the flow separation. While not large, this zone has a significant influence on base drag and base heat transfer. The near wake may be divided into the recirculation region and the free rear-stagnation

point. In the transition region, the vortex streets are in the process of breaking down and the flow becomes turbulent and develops into similar velocity profile. In the similarity or far-wake region, the flow becomes completely turbulent and the velocity profiles are similar in each section. In this region the flow is dominated by large-scale turbulent structure, has well-established equilibrium characteristics and the energy spectrum of the velocity fluctuations approaches that of isotropic turbulence. The overall structure of the wake depends on many parameters such as Reynolds and Mach numbers and the geometric form of the body.

Recent advances in stability theory and related experiments have shown that the vortex formation region is one of global absolute instability, see, e.g., [1,2, 3]. The shear layer of the wake is characterized by a change in the instability properties from locally absolute to locally convective at a particular downstream location. A flow is absolutely unstable if disturbance waves, generated by a pulse wise perturbation contain amplified upstream- and downstream-traveling waves as well as one that remains at the location of its generation, while amplifying in time. One consequence of absolute instability is that each local disturbance that is introduced will, with progression of time, influence the complete flow field. On the other hand, if the flow is convectively unstable, amplified disturbance waves are convected away from the location of generation; after a sufficiently large time the basic flow is again locally-undisturbed.

Koch [4 & 5] suggested that the shedding frequency of the wake is governed by a direct local resonance, occurring at the location where the transition from absolute to convective instability takes place and caused by the coalescence of an upstream- and a downstream-traveling mode. This hydro-mechanical resonance mechanism is the key to the frequency selection of vortex shedding and to vortex control. The existence of the absolutely unstable region makes effective wake control accessible.

The external disturbances represent potential means for active control of the bluff-body near-wake flow. Active control of the vortex shedding in the wake of a stationary circular cylinder by means of acoustic feedback was demonstrated in [6]. Passive control of the shedding process, which can be accomplished by geometric alterations by means of splitter plates, special trailing-edge configurations, serrated trailing edges and base bleed, have been known and experimentally tested for decades, see, e.g., the review articles [1,7,8].

Modification and control of the bluff-body wake flow can be employed either, to reduce the intensity of turbulence in the wake in order to reduce drag or, to intensify turbulence in the wake flow in order to enhance heat transfer, mixing and combustion. Available information on the velocity and turbulence characteristics of wake flows with recirculation is limited, and even not existing, for perforated disks. For solid disks, [9] refers to a recirculation length of 2.5 disk diameter, D, while [10] quotes a value of 2 D. Calvert [11] refers to the presence of definite periodicity corresponding to a Strouhal number of 0.19. Durão and Firmino [12] report a recirculation length of 1.35 D and periodic oscillations corresponding to a Strouhal number of 0.18.

The present investigation was motivated by the desire to extend the knowledge of the aerodynamic characteristics of axisymmetric turbulent wake flows behind circular disks with a central perforation that may be used for passive wake control.

The present experimental measurements were undertaken using three separate perforated disks having a central-hole/disk diameter ratios (d/D) of 0.17, 0.27 and 0.37. The mean velocities and turbulence characteristics, as major objectives, have been measured with a constant-temperature hot-wire anemometer. For all observations, the Reynolds number of the undisturbed oncoming flow (based on the disk diameter D) was kept around 3.6×10^4.

The present work also includes a numerical investigation of the turbulent wake flow behaviour using a finite-volume-based computational model. A two-equation turbulence model with different variants was tested and their results are compared to experimental measurements.

2. EXPERIMENTAL ARRANGEMENT AND INSTRUMENTS

The experiments were conducted in the open-circuit subsonic wind tunnel, located in the Aerodynamics Laboratory of Ain Shams University. The essential features of the system are shown in Fig. 1. Air is drawn into the entrance part, settling section comprising a honeycomb and graduated screens, through the contraction (having an area ratio of 6.25) and the test section, expanded in the diffuser section, propelled through the fan and finally exhausted through the diffuser silencer to the atmosphere.

The wind-tunnel fan is axial type, belt driven by an externally-mounted 10-hp AC induction motor. The motor speed is regulated by a transistor inverter-type variable-speed controller. The ducts bounding the flow are fabricated from fiberglass reinforced plastic laminated over-precision molds. The plexiglass test section is fitted with a

removable side port secured with quick release fasteners. The port is kept closed tightly during operation. The interior physical dimensions of the test section are: height 305 mm, width 305 mm and length 610 mm. The top of the test section is arranged to support the traversing mechanism. The undisturbed average air velocity, U_o, in the test section could be varied in the range from 3 to 55 m/s. The maximum freestream turbulence intensity $\left(u'/U_o\right)$ is less than 0.5 %, where $\left(u' = \sqrt{\overline{u^2}}\right)$ is the root-mean-square value of the fluctuating velocity component.

The test models are three brass disks with central hole diameter d = 5, 8 and 11 mm, each disk has a diameter D = 30 mm and thickness t = 4 mm. The disks are sharp-edged from upstream and downstream faces. Each of the three disks was held in the center of the test section by four piano wires of 0.3 mm diameter. The disk presents an area blockage to the approaching stream of less than 1 %. The disks were placed normal to a stream of undisturbed average velocity 20 m/s.

Mean velocities and turbulence intensities were measured with a constant-temperature hot-wire anemometer (CTA) as a part of the measuring system. The measuring system comprises a personal computer equipped with a GPIB interface board, an analog to digital converter, the hot wire probes, the CTA bridge, the control and traversing interface and the automatic traversing mechanism.

The X-wire sensor probe, Dantec 55P51 model, was used to measure the mean velocities and root-mean-square turbulence intensities in two coordinate directions. The X-wire probe has two sensors aligned perpendicular to each other, and in two parallel planes. The probe stem is aligned with the axial direction parallel to the planes of the two sensors and bisects the 90° angle formed by the two sensors. The sensing elements were made of 5 μm diameter platinum-coated tungsten wire. The wires were welded at the ends of two gold prongs 9.1 mm long. The prongs are molded in ceramic stems 2.3 mm in diameter and 33 mm in length. The probe is mounted on a 6 mm diameter support. The probe wires are connected to Wheatstone bridges. The Wheatstone bridges and servo amplifiers are the main components of the constant-temperature hot-wire bridge, Dantec CTA 56C. The automatic traversing mechanism used is Dantec 56H00 series with Dantec 57G15 interface frame. The National Instruments MC-GPIB card is used to interface the personal computer with Dantec 56H00 traversing mechanism.

The hot wire sensors were calibrated using Dantec 92D190 calibration facility. The calibration process consists of tabulating a set of calibration points by assigning reference values to the variable being calibrated. A continuous relationship between the reference velocities and the output voltage from the CTA bridge is provided by a calibration polynomial which is computed by a curve fitting technique. This calibration polynomial function is integrated with data processing operations carried out by the data acquisition program to yield the measured fluid velocity components.

The mean velocities and root-mean-square turbulence intensities in the axial and radial directions were determined along the centerline and across the wake, at longitudinal positions up to 8 disk diameters, by means of the X-wire probe. Diametrical traverses about the centerline, irrespective of their axial position, were performed to check for the axial symmetry of the mean flow pattern.

From the literature, it is clear that the main feature of flows similar to the one under investigation is the existence of a recirculating zone, see e.g. [9,10,11,12]. Since the hot-wire anemometer gives no indication of the sign of the velocity, thus, inside recirculation regions, the sign at each experimental point must be decided by inspection. This is achieved by utilizing a mirror imaging technique to modify the sign of the observed velocitiy values, see [11].

3. MATHEMATICAL FORMULATION AND CALCULATION PROCEDURE

3.1 Governing Equations

The system of equations governing the time-averaged, steady, isothermal, incompressible, turbulent axisymmetric flow field in the cylindrical coordinates is expressed as follows.

The continuity equation

$$\frac{\partial U}{\partial x} + \frac{1}{r}\frac{\partial (rV)}{\partial r} = 0 \qquad (1)$$

The momentum equations

$$\rho \frac{DU}{Dt} = -\frac{\partial P}{\partial x} + \frac{\partial}{\partial x}\left(2\mu S_{xx} - \rho\overline{u^2}\right) + \frac{1}{r}\frac{\partial}{\partial r}\left[r\left(2\mu S_{xr} - \rho\overline{uv}\right)\right] \qquad (2)$$

$$\rho \frac{DV}{Dt} = -\frac{\partial P}{\partial r} + \frac{\partial}{\partial x}\left(2\mu S_{xr} - \rho\overline{uv}\right) + \frac{1}{r}\frac{\partial}{\partial r}\left[r\left(2\mu S_{rr} - \rho\overline{v^2}\right)\right] - \frac{1}{r}\left(2\mu S_{\theta\theta} - \rho\overline{w^2}\right) \qquad (3)$$

where the substantial derivative operator $\frac{D(\ )}{Dt} = U\frac{\partial(\ )}{\partial x} + V\frac{\partial(\ )}{\partial r}$ in the steady state

conditions. In the above equations, U and V represent the time-mean velocity components in the axial and radial directions, respectively, ρ is the fluid density, μ is the fluid dynamic viscosity and P is the time-mean static pressure. The term S_{ij} is regarded as the fluid mean rate of strain tensor, where the axes in the directions x, r, θ are labeled 1, 2, 3 respectively. The elements of the strain tensor are

$$S_{xx} = \frac{\partial U}{\partial x},\ S_{rr} = \frac{\partial V}{\partial r},\ S_{\theta\theta} = \frac{V}{r} \text{ and}$$

$$S_{xr} = \frac{1}{2}\left(\frac{\partial U}{\partial r} + \frac{\partial V}{\partial x}\right) \qquad (4)$$

The terms $\overline{u^2}$, $\overline{v^2}$, $\overline{w^2}$ and $\overline{uv}$ are the non-zero elements of the second moment tensor $\overline{u_i u_j}$. The turbulent or Reynolds stress tensor is given by $-\rho\overline{u_i u_j}$.

3.2 Turbulence Modeling

Since the Reynolds stresses $-\rho\overline{u_i u_j}$ appear as unknowns in Eqs. (2 & 3), additional equations are needed to solve the above system of equations. The k-ε model is the widest applied two-equation eddy-viscosity model and is employed in the present study along with some variants which are tested to procure better performance in flows with strong curvature.

In the k-ε model, the Boussinesq's eddy-viscosity concept is used, and the Reynolds stress is defined as

$$-\rho\overline{u_i u_j} = 2\mu_t S_{ij} - \frac{2}{3}\delta_{ij}\rho k \qquad (5)$$

where μ_t is the eddy or turbulent viscosity, k $\left(= \overline{u_i u_i}/2\right)$ is the turbulence kinetic energy and δ_{ij} is the Kronecker delta $\left(= 1 \text{ for } i = j \text{ and } = 0 \text{ for } i \neq j\right)$. The formulation for the eddy viscosity used in the standard k-ε model is given as

$$\mu_t = C_\mu \rho k^2 / \varepsilon \qquad (6)$$

where ε, the dissipation rate of k, is written as:

$$\varepsilon = \nu\overline{\left(\frac{\partial u_i}{\partial x_j}\right)^2} \qquad (7)$$

and ν is the kinematic viscosity of the fluid.

The distribution of k and ε is determined from the solution of the semi-empirical transport equations which, in the standard k-ε model, are as follows:

Transport of turbulence kinetic energy k

$$\rho\frac{Dk}{Dt} = \frac{\partial}{\partial x}\left[\left(\mu + \frac{\mu_t}{\sigma_k}\right)\frac{\partial k}{\partial x}\right] + \frac{1}{r}\frac{\partial}{\partial r}\left[r\left(\mu + \frac{\mu_t}{\sigma_k}\right)\frac{\partial k}{\partial r}\right] + G - \rho\varepsilon \qquad (8)$$

Transport of rate of turbulent dissipation ε

$$\rho\frac{D\varepsilon}{Dt} = \frac{\partial}{\partial x}\left[\left(\mu + \frac{\mu_t}{\sigma_\varepsilon}\right)\frac{\partial \varepsilon}{\partial x}\right] + \frac{1}{r}\frac{\partial}{\partial r}\left[r\left(\mu + \frac{\mu_t}{\sigma_\varepsilon}\right)\frac{\partial \varepsilon}{\partial r}\right] + P_\varepsilon - C_2\rho\frac{\varepsilon^2}{k} \qquad (9)$$

where G is the production rate of turbulence kinetic energy expressed as

$$G = -\rho\overline{u_i u_j} S_{ij} \qquad (10)$$

and P_ε is the production of the dissipation rate of k expressed as

$$P_\varepsilon = C_1 G\frac{\varepsilon}{k} \qquad (11)$$

The empirical constants appearing in Eqs. (6, 8, 9 & 11) take the standard values recommended by [13], namely $C_\mu = 0.09$, $\sigma_k = 1.0$, $\sigma_\varepsilon = 1.3$, $C_1 = 1.44$ and $C_2 = 1.92$, which satisfy the limiting behaviour of isotropic turbulence and turbulence at local equilibrium.

Since the k-ε model in its standard form does not account for important secondary strain effects such as those resulting from curvature, therefore it is essential to include some modifications. The main objective of these modifications is to yield the lower eddy viscosity values necessary for a correct prediction of recirculating flows. Three modifications of the standard k-ε model were considered in the present study.

(i) The first modification is the streamline curvature modification. It accounts for effects of streamline curvature on turbulence and has been derived by simplification of an algebraic Reynolds-stress model, as described in [14]. This modification involves a calculation of the empirical constant C_μ as follows

$$C_\mu = \frac{K_1}{1 + 8K_2^2 \frac{k^2}{\varepsilon^2}\left(\frac{\partial U_s}{\partial n} + \frac{U_s}{R_c}\right)\frac{U_s}{R_c}} \qquad (12)$$

where $K_1 = 0.09$, $K_2 = 0.267$, U_s is the local velocity in the streamline direction and n is the direction normal to it, as shown in Fig. 2. The local radius of curvature of the streamline R_c is evaluated using differential calculus from the following equation [15].

$$\frac{1}{R_c} = \frac{UV\left(\frac{\partial V}{\partial r} - \frac{\partial U}{\partial x}\right) + U^2\frac{\partial V}{\partial x} - V^2\frac{\partial U}{\partial r}}{\left(U^2 + V^2\right)^{3/2}} \qquad (13)$$

The magnitude of U_s is simply obtained from a vectorial summation of U and V, and care has to be taken with respect to the sign. This is determined by examining the signs of U and V in relation to the sign of R_c. Since the rate of shear strain in the streamline coordinate system is given by

$$S_{ns} \cong \frac{\partial U_s}{\partial n} - \frac{U_s}{R_c} \qquad (14)$$

and for an angle of rotation ϕ, between the velocity vector and the x-axis, S_{ns} is related to the rate of strain tensor as follows

$$S_{ns} = (S_{rr} - S_{xx})\sin 2\phi + 2S_{xr}\cos 2\phi \qquad (15)$$

Using Eqs. (13, 14 & 15) the gradient $\partial U_s / \partial n$ could be determined.

As pointed out in [16], the correction of C_μ, described by Eq. (12), leads to a significant reduction in its value around the curved shear layer bordering the recirculation zone. Within this zone C_μ would tend to zero or even reverse sign if a lower limit is not placed. This limit was arbitrarily chosen as in [16] to be 0.025. As mentioned also in the same reference, in regions where C_μ is below this value, the concept of local equilibrium on which the curvature correction is based cannot be expected to hold.

(ii) The second modification is the preferential dissipation modification, originally proposed in [17]. This modification recommends the addition of an extra term to the transport equation for ε to account for the preferential influence of normal stresses over shear stresses in promoting the transfer of turbulent energy from large to small eddies and thereby increasing the rate of dissipation in flows with strong curvature. The modification implies the replacement of the production-of-dissipation term P_ε in Eq. (9) by the term

$$P_\varepsilon = \left(C_1' G - C_1'' \mu_t S_{ns}^2\right)\frac{\varepsilon}{k} \qquad (16)$$

The values of the constants $C_1' = 2.24$ and $C_1'' = 0.8$ were adopted to insure that, in the absence of streamline curvature, the shear production of ε will be identical to that in the standard k-ε model, i. e., $C_1' - C_1'' = C_1$.

(iii) The last modification investigated is simply the combination of the above two.

4. COMPUTATIONAL DETAILS AND BOUNDARY CONDITIONS

4.1 Numerical Model

A finite-volume formulation is used to derive algebraic approximations to the set of governing elliptic partial differential equations with the associated boundary conditions. A staggered nonuniform grid arrangement, with velocity nodes offset from scalar nodes, is used in the present computations as shown in Fig. 3. The grid layout adopted has centered volume faces in which the control volume faces are placed midway between the grid points. The discretization scheme used is the hybrid central/upwind difference scheme for linking the convection and diffusion terms. In this scheme, the upwind-difference part is used if the grid Peclet-number in a given direction exceeds 2 and the central-difference part is otherwise used, [18]. This scheme gives what may be termed a physically realistic solution. In other words, the shortcomings of the central-difference and upwind schemes are not shared by the hybrid scheme.

The domain of solution considered extended to an upstream distance of 10D, to a downstream distance of 15D and to a radius of 5D. The locations of these boundaries were determined after several computations to insure that they have no noticeable effect on the flow in the recirculation region. A proper resolution of the region immediately around the disk was found particularly critical to the accuracy of the solution. Consequently, a cluster of fine grids was located at this region with minimum grid sizes of $\Delta x_{min}/D = 0.8\ \%$ and $\Delta r_{min}/D = 0.6\ \%$. Figure 4 shows typical grids that are generated for the present flow computations.

To minimize the truncation errors associated with nonuniform grid distribution, the effect of the grid expansion factors $E_x = \Delta x_i / \Delta x_{i-1}$ and $E_r = \Delta r_j / \Delta r_{j-1}$ was investigated. It was found that a reliable solution could be obtained, without

loss of accuracy, if these expansion factors are kept within the following ranges

$$0.8 \le E_x, E_r \le 1.2 \ \ for \begin{cases} -1 \ge x/D \ge 3 \\ r/D \ge 1 \end{cases} \quad (17)$$

$$0.9 \le E_x, E_r \le 1.1 \ \ for \begin{cases} -1 \le x/D \le 3 \\ r/D \le 1 \end{cases} \quad (18)$$

4.2 Boundary Conditions

For the flow geometry under consideration, the computational domain boundaries were set as follows, see Fig. 5.

(i) At the inlet boundary (AB), uniform flow conditions are imposed for all variables using experimental inlet conditions:

$$U = U_o, \ V = 0, \ k_o = \frac{3}{2}\overline{u_o^2} \text{ and } \varepsilon_o = \frac{k_o^{3/2}}{\lambda W} \quad (19)$$

where $\overline{u_o^2}$ is specified to correspond to a uniform isotropic turbulence intensity of 0.5 %. Following the recommendation of [19], a value of $\lambda = 0.005$ is prescribed, where W is the wind tunnel width.

(ii) Along the symmetry axis (BC), a zero cross-stream gradient condition, $\partial(\ )/\partial r$, is specified for all variables with V = 0.

(iii) The no-slip boundary conditions are imposed along solid boundaries (AD, EF, FG, GH and HE). According to [13], and in the absence of better information, the diffusion of k to the wall is set equal to zero, or $\partial k/\partial y = 0$. The near-wall values of the parallel velocity component, the turbulent kinetic energy and its dissipation rate are specified by the wall shear stress based on the wall-function approach [13]. This approach is usually used to bridge the gap between the fully turbulent region and the wall. In the derivation of the wall function, y^+ and U^+ are taken as the nondimensional normal distance and resultant velocity parallel to the wall, respectively, defined as

$$y^+ = \rho y U_\tau / \mu, \ U^+ = U_{res}/U_\tau \text{ where } U_\tau = \sqrt{\tau_w/\rho} \quad (20)$$

In the equilibrium layer near the wall, the production of k is in balance with its dissipation rate. Assuming that the dominant term in the near wall production of k is the shear stress, which is nearly constant, the following expression can be derived using Eqs. (5, 6, 8 & 10).

$$\tau_w = C_\mu^{1/2} \rho k \quad (21)$$

The dimensionless velocity parallel to the wall is calculated from the universal velocity profile,

$$U^+ = y^+ \quad \text{for the viscous layer } (y^+ < 11.63) \quad (22a)$$

$$U^+ = \frac{1}{\kappa}\ln\left(Ey^+\right) \quad \text{in the fully turbulent region } (y^+ > 11.63) \quad (22b)$$

where von Kármán constant κ and E are the log-law constants and equal to 0.4187 and 9.793, respectively.

Using Eqs. (10 & 22b), the near wall production of k can be represented as follows:

$$G = \rho U_\tau^3 / (\kappa y) \quad (23)$$

Referring to Fig. 6, the production of k for a given finite volume that lies immediately adjacent to the wall is obtained by integrating Eq. (23) over the region occupied by the node P next to the wall. Based on the assumption that the flow is in local equilibrium in the near wall region, $\rho\varepsilon = G$, the value of ε at y_P is simply expressed as

$$\varepsilon_P = U_\tau^3 / (\kappa y_P) \quad (24)$$

Equation (24) replaces the transport equation for ε, namely Eq. (9), at the nodes that lie immediately adjacent to the wall.

(iv) The outlet boundary (CD) is positioned at a location where for all grid points next to it the Peclet number is sufficiently large. In this case the region near the outflow boundary exhibits a local one-way behaviour. In other words the value of a variable at any point will be uninfluenced by any of the downstream values.

4.3 Solution Procedure

The set of difference equations were solved iteratively using the solution algorithm outlined in [18], incorporating the semi-implicit method for pressure-linked equations. The code uses a line-by-line solution procedure which is a combination of the tridiagonal matrix solver and Gauss-Seidel technique. Underrelaxation factors were used to promote stability with values of 0.5, 0.5, 0.7 and 0.6 for U, V, k and ε, respectively. The turbulent viscosity field was underrelaxed with a value of 0.25, whereas no relaxation was applied to the pressure correction field.

It should be noted that, referring to Fig. 6, the value of k_P is calculated from the regular balance equation for k in each iteration step. Such value of k_P is necessary to assign a value for y_P^+ via Eqs. (20 & 21). Since the k-ε model is only valid in the

fully turbulent region, care has to be taken to ensure that the first grid line adjacent to the wall lies at a distance $y_P^+ > 11.63$ where Eq. (22b) is applied. If during the iteration process the value of y_P^+ drops below 11.63, Eq. (22a) is employed. The iteration cycle is terminated and the solution is considered converged, when the overall mass and momentum residuals, normalized using inlet conditions, reach a value of less than 0.5 %.

The mesh size was determined by conducting a grid independence study on the solution. Grid independence was established by examining the cross-stream velocity distributions at the middle of the recirculation zone. For this purpose, Re was chosen to be 3.6×10^4 and for the same expansion factors, a number of different uniform and nonuniform grid distributions were investigated. Grid independence was attained when maximum changes in velocity distribution were less than 2 %. The present computations were performed on a Pentium-233 Mhz personal computer having 64 MB RAM. For a (160 × 140) grid, each run required about 160 minutes of CPU time and about 2800 iterations.

5. RESULTS AND DISCUSSION

5.1 Preliminary Computations

In order to assess the capability of two-equation models to predict perforated disk wake flow, preliminary computations were performed for solid disks. These predictions are compared with available experimental measurements from several sources.

Figure 7 shows the predicted variation of normalized centerline mean velocity U_{cl}/U_o, for a solid disk at Reynolds number of 3.6×10^4 using different models. The figure also includes experimental measurements for different values of Reynolds number ranging from 4×10^4 to 7×10^4. As can be seen in the figure, the experimental measurements show that the centerline velocity is negative in the downstream region of the disk up to x/D = 3. This region corresponds to the recirculation zone behind the disk. In this region the maximum negative velocity is attained at x/D = 1.5. The maximum negative velocity along the centerline is about half the free stream velocity U_o.

The standard k-ε model predicts a very small negative velocity which quickly disappears after x/D = 0.5. This is followed by a fast recovery of the centerline velocity which becomes nearly 90% of U_o at x/D = 2. This behaviour is indicative of a fast diffusion rate of momentum towards the wake centerline. The k-ε model clearly overestimates the value of the eddy viscosity, and the associated turbulence levels in the initial shear layer of the wake which results in this fast diffusion rate.

The preferential model results in a better agreement with the experimental measurements in the recirculation zone, Fig. 7. This model predicts the correct value of maximum negative velocity. However, the recovery of the centerline velocity is as fast as that predicted by the k-ε model. This results in predicting a too narrow recirculation region, compared with the experiments

The predictions obtained using the curvature effect model, also shown in Fig. 7, are in closer agreement with the experimental measurements. This is reflected in the wider length of the recirculation zone predicted by this model, as well as the maximum negative velocity, which nearly match the measured values. However, the velocity recovery rate is slightly slower than the experimental data.

The combined model uses both the preferential-effect and the curvature-effect models. This model is clearly overestimating the effects of curvature in the solid disk case. Fig. 7.

Figure 8 shows the predicted variation of the centerline mean static pressure coefficient obtained, by the four models discussed above, and defined as follows:

$$C_P = \frac{P_{cl} - P_o}{\frac{1}{2}\rho U_o^2} \qquad (25)$$

As can be seen in the figure, the k-ε model predicts large negative static pressure behind the disk. The predictions of the curvature model and the combined model are in good agreement with the experimental measurements.

In the following test cases of perforated disks only the curvature model and the combined model shall be used in the predictions. For all computations reported here the inlet velocity was prescribed as uniform at U_o = 20 m/s, while the disk outer diameter was chosen to be D = 30 mm.

5.2 Perforated Disk Cases

Figure 9 shows the measured variation of the normalized centerline velocity U_{cl} / U_o for the perforated disk cases. For comparison, the figure also shows the measurements for the solid disk case at equal Reynolds number reported in [20]. As can be seen in the figure, for perforated disks, the centerline velocity near the disk is positive and decays gradually until it attains a minimum value x/D ≅ 2. For disks with 8 mm and 11 mm hole diameters the centerline velocity close to the disk exceeds the free stream velocity U_o. This increase can be justified due to the acceleration of the fluid

upstream the disk into the central hole. For the 5 mm hole diameter case, the centerline velocity downstream the disk is only 60 % of the free stream velocity value. Thus, reducing the hole diameter below 8 mm clearly affects the value of the centerline velocity downstream the disk. After x/D = 3, all wakes exhibits similar behaviour of the centerline velocity recovery rate.

Figures 10 (a - c) show the predicted variation of the centerline velocity for the three perforated disk cases using the curvature model and the combined model, compared with the experimental measurements. The predicted decay of the centerline velocity in the near region matches the experimental behaviour. However, contrary to the experimental measurements, both models predict negative centerline velocity in the near wake region. This defect indicates that the correction of turbulent diffusion in regions with curved streamlines is excessive. The positive jet momentum issuing from the disk hole diffuses at a fast rate which is unaffected by the correction term. Outside the jet region, diffusion of momentum from the external stream is weak and does not prevent the centerline velocity to become negative.

Figure 11 (a) shows the predicted wake normalized streamwise mean velocity profiles U / U_o at different downstream positions, also compared with the experimental measurements, for the perforated disk with 5 mm hole diameter. The combined model predicts better agreement with the measurements in the near field. At x/D = 0.5, both models predict slightly higher positive velocity at the centerline. The profile is generally in agreement with the measurements. Both models predict negative velocities, indicating recirculating regions. However, the experimental measurements indicate positive velocities across the whole wake. This flow pattern resembles the weak jet-wake interacting flow. The effects of jet entrainment can be the reason of the absence of any recirculation in the core region of the wake. Figures 11 (b) and (c) show the predictions obtained for the remaining cases with hole diameter d = 8 and 11 mm. Again, both models predict negative velocities in the core region of the wake, which were not observed in the experiments. At x/D = 3, the predictions show a lower centerline velocity, compared with the measurements.

Figure 12 shows the measured and predicted variation of streamwise turbulence intensity, at the centerline u'_{cl}/U_o with x/D for the three cases investigated in this study. As can be seen, increasing the hole diameter of the disk results in a slower rise up of the centerline turbulence intensity. For d = 5 mm, the peak centerline intensity is reached at x/D ≅ 0.5. For the cases with d = 8 and 11 mm, the peak centerline intensity is reached at x/D ≅ 1.5.

After reaching the peak value, the centerline turbulence intensity decays at a fast rate and rises again to form a secondary peak. The magnitude of the secondary peak is lowest for the largest perforation diameter d = 11 mm. It is interesting to note that the decay rate at this stage is almost identical for the three cases. The effect of the initial upstream conditions starts to disappear after the secondary peak.

The predictions of the centerline turbulence intensity, using both the curvature and combined models, show a faster rise of turbulence intensity near the disk. Both models predict the first peak at the same location regardless of the disk hole diameter. The decay rate after this peak is also fast and the predictions become close to the measurements at x/D ≅ 1 – 1.5. In general, the combined model results are in better agreement with the measurements. Both models predict a slower decay rate far from the disk. At this region, curvature effects are nearly negligible and both models must give similar results since they revert to the standard k-ε model.

The measurements and predictions of the turbulence intensity profiles, u'/U_o are shown in Figs. 13 (a - c) for the perforated disk cases at different downstream positions up to x/D = 8. For d = 5 mm, Fig. 13 (a), the combined model predictions are in better agreement with the experiments. Both models predict a peak value of turbulence intensity in the shear layer of the separating stream, which is confirmed by the measurements. In this region, the strong shear rate is responsible for this peak turbulence intensity. This peak diffuses in the cross-stream direction as the flow develops. For larger hole diameters, Figs. 13 (b) and (c), the centerline peak turbulence intensity becomes more important due to the creation of another strong shear layer at the edge of the fluid jet passing through the disk hole. Both models overpredict the centerline peak close to the disk. Further downstream, the models predictions become in better agreement with the measurements.

Figure 14 (a) shows the measured and predicted mean velocity profiles, at x/D = 8, plotted in similarity coordinates. The figure also shows the well-established equation for similar velocity profiles in the developed wake, first obtained by [31].

$$\frac{U_o - U}{U_o - U_{cl}} = \left[1 - 0.3 \left(\frac{r}{r_{1/2}} \right)^{3/2} \right]^2 \qquad (26)$$

where $r_{1/2}$ is the value of r at which the left hand side of Eq. (26) equals one half. The experimental

measurements and numerical predictions are in reasonable agreement. However, some deviation from the Swain relation is expected since, at x/D = 8, the wake has not reached complete similarity. There is also little effect of the disk hole diameter on the normalized velocity profiles using similarity coordinates.

Figures 14 (b) and (c) show the normalized streamwise turbulent stress and shear stress profiles, also plotted in similarity coordinates, at x/D = 8. The numerical results are plotted for the case with d = 8 mm, since little differences were observed between the three cases. The combined model predicts too low turbulence levels, normalized by the mean velocity defect, $\left(U_o - U_{cl}\right)$. The curvature model results are in better agreement with the measurements. The predicted shear stress profiles by both models are lower than the experimental measurements. This is consistent with the observed mean velocity slow build up and diffusion, shown in Figs. 10 and 11. The curvature-effect modification results in excessive reduction of the turbulent viscosity in the core of the shear layer, even as far as x/D = 8.

6. CONCLUSIONS

Experimental measurements and numerical predictions of mean velocity and turbulent correlations in the near wake of perforated disks have been presented and discussed.

The experimental measurements showed that, for the investigated cases with d/D ratios of 0.17, 0.27 and 0.37, no recirculation region exists in the wake region. This may be attributed to the entrainment effects of the hole jet from the fluid enclosed in the back side of the disk. The jet disappears very fast, as early as x/D = 1.5. For high values d/D the centerline mean velocities close to the disk exceeds the free stream value. This is justified by the acceleration gained by the fluid upstream the disk. The measured profiles resemble a weak jet-wake interacting flow.

The standard k-ε model fails to represent the effects of turbulence in flows dominated by curvature effects presently examined. The turbulence-model modifications accounting for the effects of streamline curvature lead to improve the agreement with the experimental data. Both the curvature and combined models predictions are generally in good agreement in the region close to the disk. However, both models predict negative velocities in the core region of the wake which are not observed in the experiments. This may be an indication to the excessive influence of the curvature-effect correction term.

The results of the present experiments demonstrate the possibility of modification and flow control in bluff body wakes by using perforated disks.

REFERENCES

1. Rockwell, D., "Active Control of Globally-Unstable Separated Flows," In ASME *Intl. Symp. on Nonsteady Fluid Dynamics* (Proc.), FED, Vol. 92, pp. 379 - 394, ASME, 1990.
2. Schumm, M., Berger, E. and Monkewitz, P. A., "Self-Excited Oscillations in the Wake of Two-Dimensional Bluff Bodies and their Control," *J. Fluid Mech*., **271**, pp. 17 - 53, 1994.
3. Griffin, O. M., "A Note on Bluff Body Vortex Formation," *J. Fluid Mech*., **284**, pp. 217 - 224, 1995.
4. Koch, W., "Organized Structures in Wakes and Jets - An Aerodynamic Resonance Phenomenon?" In *Turbulent Shear Flows 4*, Springer, 1983.
5. Koch, W., "Local Instability Characteristics and Frequency Determination of Self-Excited Wake Flows," *J. Sound Vib*., **99**, pp. 53 - 83, 1985.
6. Ffowcs Williams, J. E. and Zhao, B. C., 'The Active Control of Vortex Shedding," *J. Fluids Struct*., **3**,pp. 115 - 122, 1989.
7. Tanner, M., "Reduction of Base Drag," *Prog. Aerosp. Sci*., **16**, pp. 369 - 384, 1975.
8. Oertel, H., "Wakes Behind Blunt Bodies," *Ann. Rev. Fluid Mech*., **22**, pp. 539 - 564, 1990.
9. Carmody, T., "Establishment of the Wake Behind a Disk," ASME *J. of Basic Engineering*, pp. 869 - 882, Dec. 1964.
10. Winterfeld, G., "On Processes of Turbulence Exchange Behind Flame Holders," *Proc. 10th Symp. (Int.) on Combustion*, p. 1265, 1965.
11. Calvert, J. R., "Experiments on the Low-Speed Flow Past Cones," *J. Fluid Mech*., **27**, part 2, pp. 273 - 289, 1967.
12. Durão, D. F. G. and Firmino, F. C., "Velocity Characteristics of the Flow Around Disks and Cones," ASME *J. of Fluids Engineering*, **106**, pp. 167 - 172, 1984.
13. Launder, B. E. and Spalding, D. B., "The Numerical Computation of Turbulent Flow," *Comp. Meths. Appl. Mech. Engng.*, **3**, pp. 269 - 289, 1974.
14. Gibson, M. M., "An Algebraic Stress and Heat-Flux Model for Turbulent Shear Flow with Streamline Curvature," *Intl. J. of Heat and Mass Transfer*, **21**, pp. 1609 - 1617, 1978.
15. Khodadadi, J. M. and Vlachos, N. S., "Experimental and Numerical Study of Confined Coaxial Turbulent Jets," AIAA *Journal*, **27**, No. 5, pp. 532 - 541, 1989.
16. Leschziner, M. A. and Rodi, W., "Calculation of Annular and Twin Parallel Jets Using Various Discretization Schemes and

Turbulence-Model Variations," ASME *J. of Fluids Engineering*, **103**, pp. 352 - 360, 1981.
17. Hanjalic, K. and Launder, B. E., "Preferential Spectral Transport by Irrotational Straining," *In Turbulent Boundary Layers*, ASME, pp. 101 - 110, 1979.
18. Patankar, S. V., "Elliptic Systems: Finite Difference Method I," In *Handbook of Numerical Heat Transfer*, pp. 215 - 240, John Wiley & Sons, Inc., 1988.
19. Cebeci, T., Khalil, E. E. and Whitelaw, J. H., "Calculation of Separated Boundary-Layer Flows," *AIAA J.*, **17**, No. 12, pp.1291 - 1292, 1979.
20. Selim, M. A., "Structure of Turbulent Wakes behind Bluff Bodies," Ph. D. Thesis, Ain Shams University, 1998.
21. Swain, L. M., "On the Turbulent Wake behind a Body of revolution," *Proc. Roy. Soc. London* A 125, p. 647, 1929.

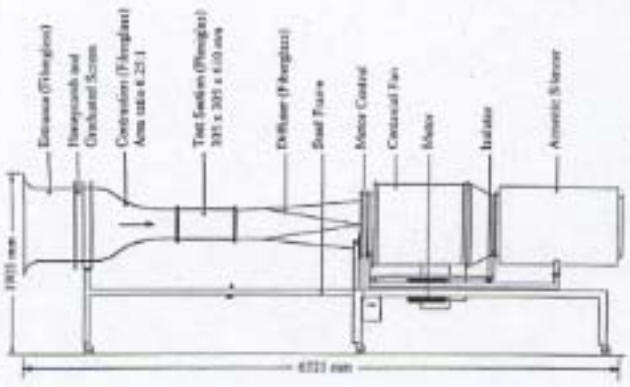

Fig. 1: Main Components of the open circuit subsonic wind tunnel

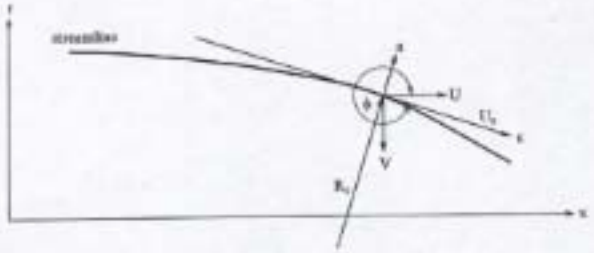

Fig. 2: Streamline coordinate system

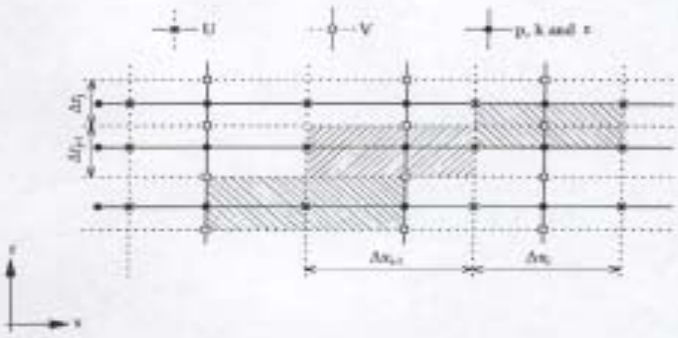

Fig. 3: Staggered grid arrangement

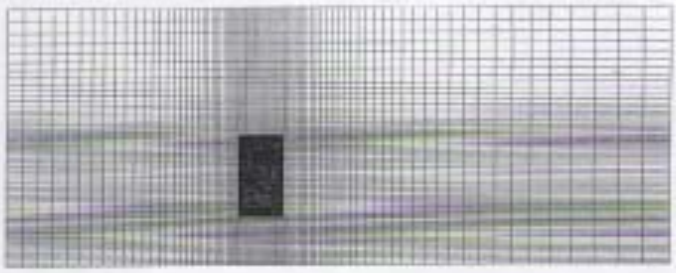

Fig. 4: Typical computational grid distribution

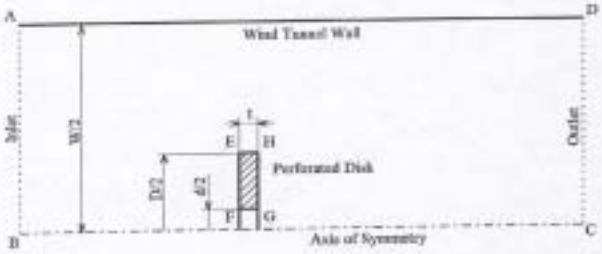

Fig. 5: Computational flow domain

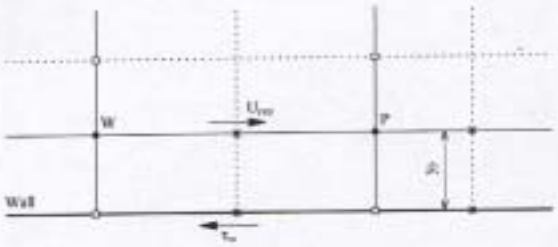

Fig. 6: Near-wall nodes

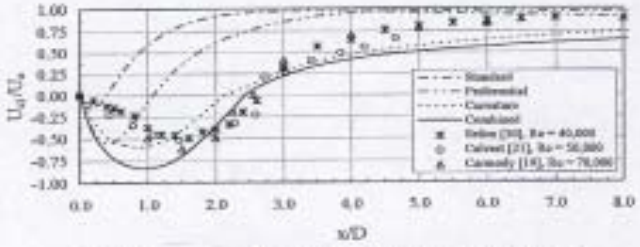

Fig. 7: Comparison of experimental and numerical centreline mean velocity variation for a solid disk.

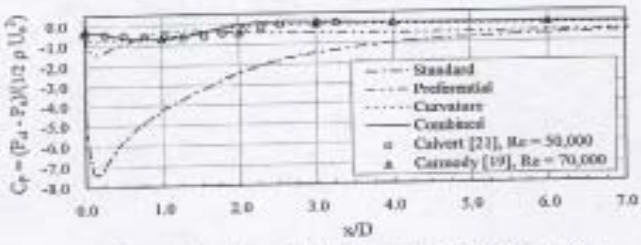

Fig. 8: Comparison of experimental and numerical centreline mean static pressure coefficient variation for a solid disk.

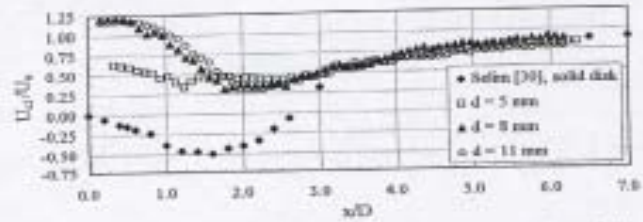

Fig. 9: Experimental centreline mean velocity variation for perforated disks.

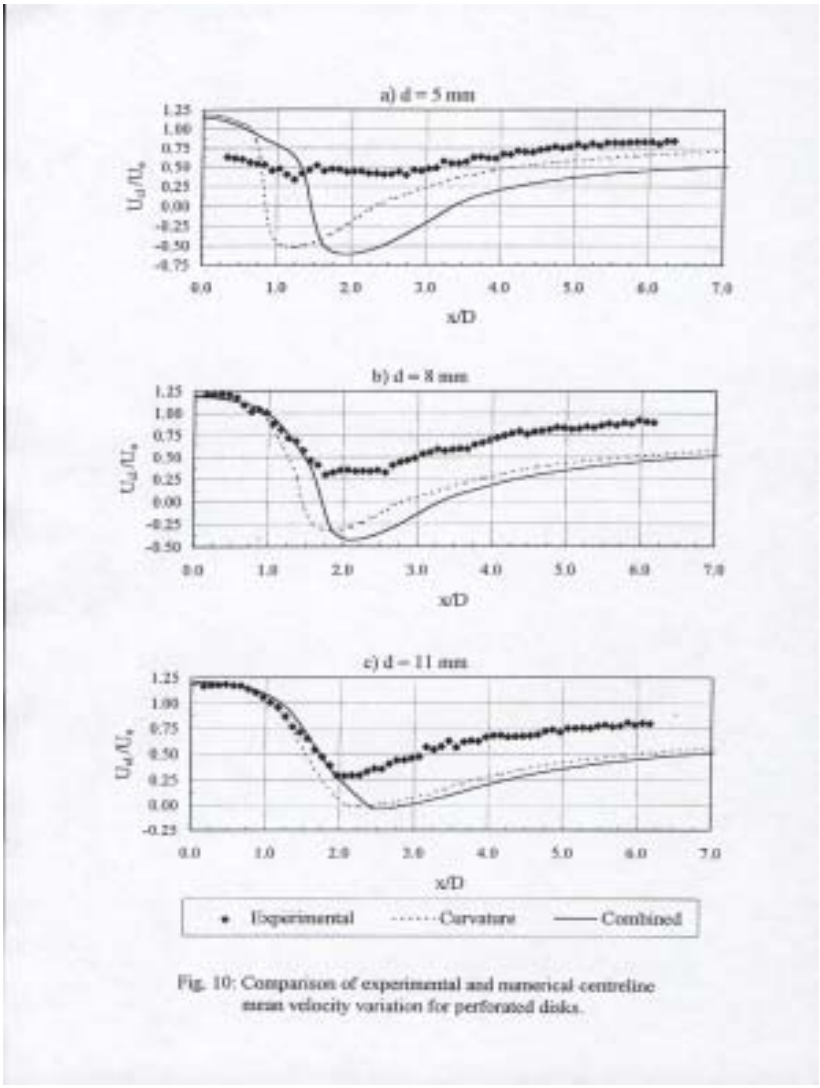

Fig. 10: Comparison of experimental and numerical centreline mean velocity variation for perforated disks.

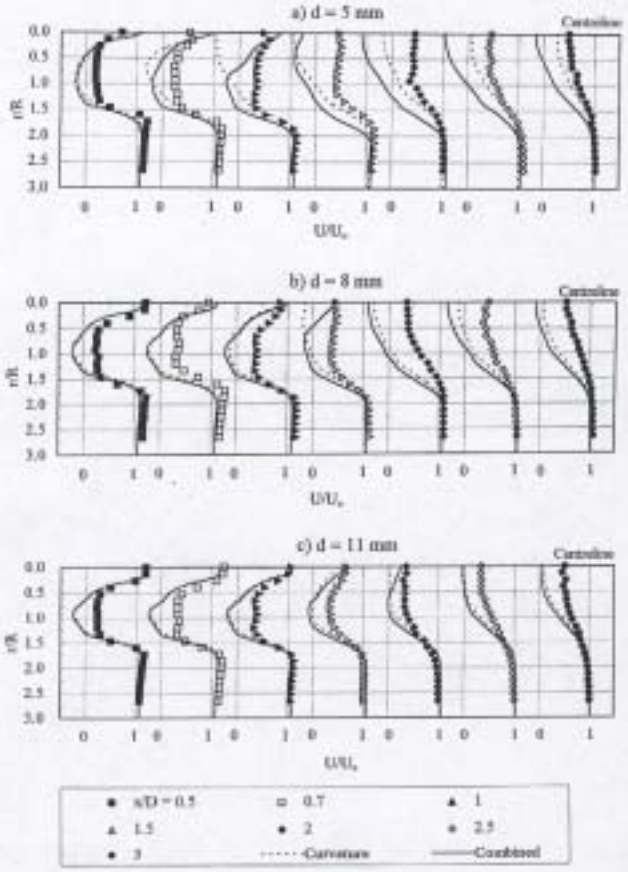

Fig. 11: Comparison of experimental and numerical mean velocity lateral profiles for perforated disks.

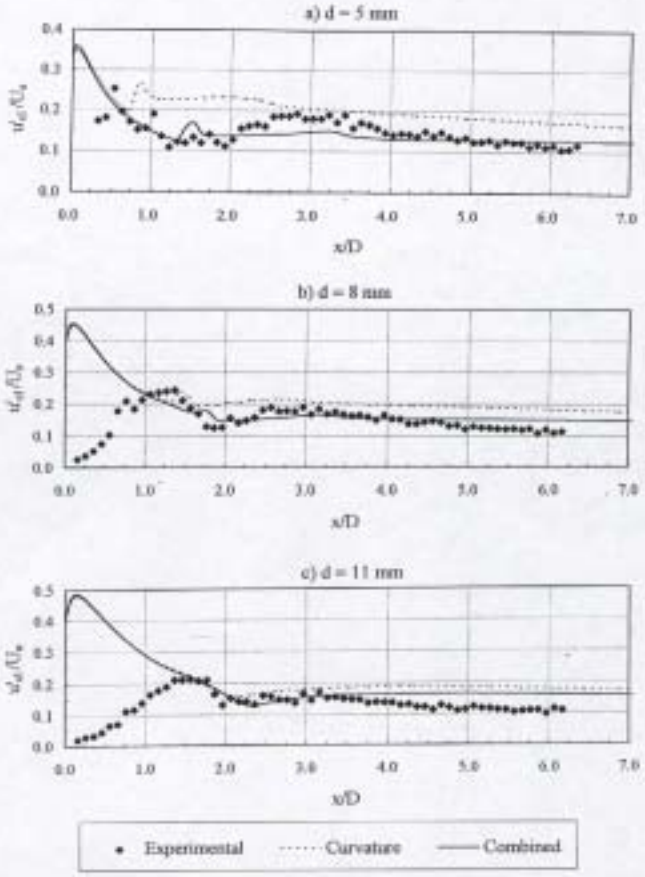

Fig. 12: Comparison of experimental and numerical centreline axial turbulence intensity for perforated disks.

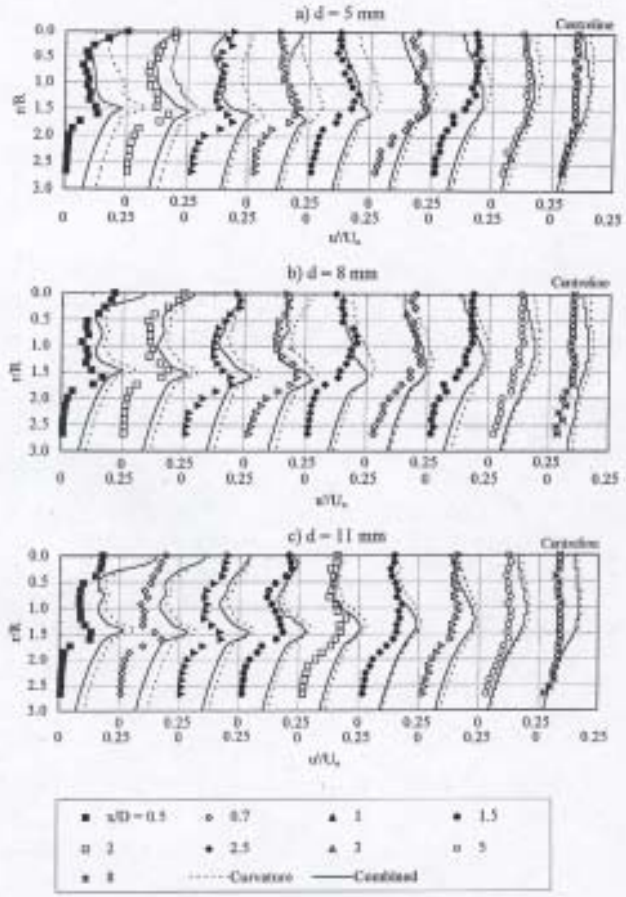

Fig. 13: Comparison of experimental and numerical axial turbulence intensity lateral profiles for perforated disks.

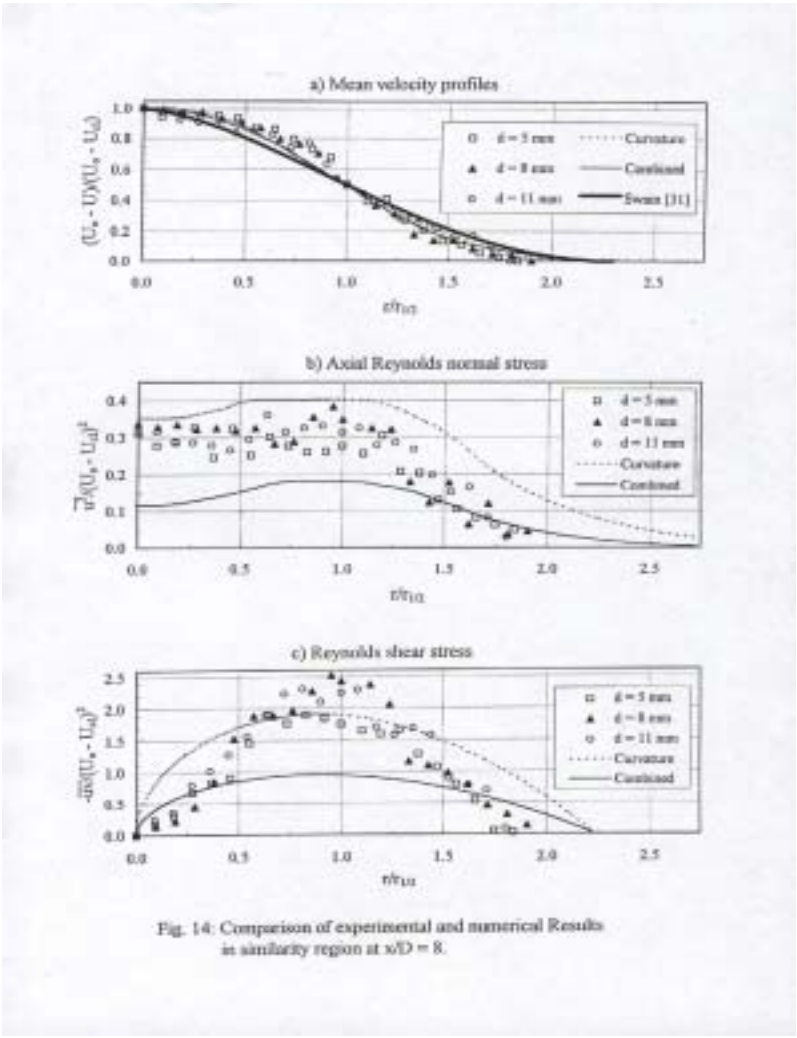

Fig. 14: Comparison of experimental and numerical Results in similarity region at x/D = 8.